Optics Letters

Experimental band flip and band closure in guided-mode resonant optical lattices

Nasrin Razmjooei and Robert Magnusson*

Department of Electrical Engineering, University of Texas at Arlington, Arlington, Texas 76019, USA
**Corresponding author: magnusson@uta.edu*

Received 10 May 2022; revised 2 June 2022; accepted 3 June 2022; posted 6 June 2022; published 29 June 2022

We demonstrate band flip in one-dimensional dielectric photonic lattices presenting numerical and experimental results. In periodic optical lattices supporting leaky Bloch modes, there exists a second stop band where one band edge experiences radiation loss resulting in guided-mode resonance (GMR), while the other band edge becomes a nonleaky bound state in the continuum (BIC). To illustrate the band flip, band structures for two different lattices are provided by calculating zero-order reflectance with respect to wavelength and incident angle. We then provide three photonic lattices, each with a different fill factor, consisting of photoresist gratings on Si_3N_4 sublayers with glass substrates. The designs are fabricated using laser interferometric lithography. The lattice parameters are characterized and verified with an atomic force microscope. The band transition under fill-factor variation is accomplished experimentally. The measured data are compared to simulation results and show good agreement.

https://doi.org/10.1364/OL.463350

The fundamental properties of solid-state materials are explained with band theory formulating propagation of electron waves in a periodic crystal lattice. Attendant Bragg diffraction leads to energy bands and bandgaps, and classification of materials as insulators and conductors [1]. Analogous bands exist in three-dimensional (3D) arrangements of periodic dielectric structures called photonic crystals [2]. The band structure showing how light propagation is affected by frequency, polarization, and direction is important in photonic crystal modeling. It is represented in the first Brillouin zone with the first and higher bandgaps corresponding the first and higher Bragg reflections with increasing frequency [3]. Photonic crystals and associated photonic band structures are the subject of considerable past and current research [2–7].

In addition to 3D periodic structures, there is immense interest in 1D and 2D optical lattices hosted by thin-film layers with parallel interfaces. The original photonic lattice, namely the 1D diffraction grating, has been around for more than 100 years. New solutions and applications based on 1D and 2D gratings consisting of spatially periodic modulations continue to appear, sometimes described as metamaterials or metasurfaces. Current lithographic technology enables fabrication of spatial modulations on subwavelength scales in one, two, or three dimensions. The resulting diffractive elements support waveguide modes if properly designed; these devices are often termed waveguide gratings in past literature. Modes that are guided, or quasi-guided, in periodic films experience stopbands and passbands as the light frequency is varied. Nano- and microstructured lattices with subwavelength periodicity support guided-mode resonance effects manifesting as resonant reflection with unit amplitude across a particular spectral bandwidth [8–12].

Guided-mode resonance (GMR) occurs when an incident wave is phase-matched to a leaky waveguide mode supported by an optical lattice. Excitation at normal incidence yields counterpropagating lateral modes producing a standing wave. Such lattices operate at the second stop band. These bands differ from 3D photonic crystal Bragg-type stop bands in that there exists an out-of-plane radiative energy-coupling channel. Therefore, the leaky mode resides above the light line in the Brillouin zone. The detailed physical and spectral properties of the resonance lattice depend critically on its symmetry. A symmetric lattice yields a single resonance and attendant radiation at one edge of the second (leaky) stop band whereas both edges resonate and radiate for asymmetric lattices. Clearly, the nonradiant edge is symmetry protected in the absence of asymmetry [8,13,14]. It cannot radiate even though its frequency is above the light line and thus connected with the radiation continuum. Taking a complex leaky-mode propagation constant $\beta = \beta_R + i\beta_I$, it was shown that symmetric structures had $\beta_I = 0$ at one edge meaning no radiation whereas asymmetric lattices had $\beta_I \neq 0$ at both edges [8]. Applying asymmetric profiles, spectral shaping by increasing the resonance grid density was implemented [13]. In 2007, a detailed study of leaky waves and bandgaps in optical lattices adopted the terminology of "nonleaky edge" for the symmetry-protected resonance and "leaky edge" for the GMR spectral location [14]. In 2008, modeling two parallel resonant lattices, the nonleaky edge became a "bound state in the continuum" or BIC [15] by drawing on analogy with bound states in quantum systems [16]. The BIC terminology is now widely accepted, and the physics of the leaky-edge BIC states is of significant scientific interest.

In prior work, it was shown that it is possible to interchange the frequency locations of the leaky and nonleaky edges [14]. The transition point is expressed in a relationship between the first (ε_1) and second (ε_2) Fourier harmonics of the periodic lattice dielectric function as $h_2 = \mathrm{Re}(h_1)$, where the coefficient $h_1 \propto \varepsilon_1^2$ and $h_2 \propto \varepsilon_2$, and the width of the stop band being $\propto |h_2 - \mathrm{Im}(h_1)|$

[17,18]. It is at this transition point that the band closes [14]. It is possible to transition to the closed-band state by design via parametric and material choices. The transition to and across this point executes a band flip whereby the leaky and nonleaky edges trade places. The band flips and bound-state transitions of simple optical lattices were studied previously using rigorous and analytical models with key aspects of the physics involved explained [18]. In more detail, the band flip and interband transition are governed by the superposition of Bragg processes denoted by $BR_{q,n}$, where q represents the Bragg order and n denotes the Fourier harmonic of the dielectric constant modulation. For small values of fill factors, the nonleaky asymmetric BIC locates at the upper band edge since the first-order Bragg reflection off the second Fourier harmonic $BR_{1,2}$ dominates the second-order Bragg reflection off the first harmonic $BR_{2,1}$ [18]. Analytical and numerical studies demonstrate that when the fill factor F increases and approaches 0.5, $BR_{1,2}$ is overwhelmed by $BR_{2,1}$, because $BR_{1,2}$ weakens as F approaches 0.5 with ε_2 simultaneously approaching zero. At this point, the bandgap closes. Before (after) the band closure, BICs appear at the upper (lower) band edge with respect to frequency. Rigorous numerical models previously applied show that the values of F where the close bands are increasingly pulled away from 0.5 as the index modulation $\Delta\varepsilon$ increases; this observation is consistent with the results presented here (with shorter wavelengths defining the upper edge).

Accordingly, the objective of this research is experimental quantification of the leaky band dynamics of lossless dielectric optical lattices. We choose the one-dimensional (1D) resonant lattice as a canonical model as it contains all key physical processes that then carryover to the 2D lattice. Numerical results illustrate the band dynamics of representative lattices via computation of spectral zero-order reflectance under variation of the angle of incidence. We explain the fabrication and characterization processes of our designs to realize this phenomenon experimentally. The theoretical and experimental results are compared showing a good match. Related research in metallic systems shows that dispersion characteristics of plasmonic particle arrays exhibit analogous leaky and nonleaky band edges [19–22] albeit governed by different physical processes.

In previous studies, band flips are investigated in designs having different dielectric constants with identical fill factors. For experimental expediency, we propose subwavelength structures having various fill factors (F). Figure 1 illustrates the band structure and band flips pertaining to two model membrane designs embedded in air. To obtain the band structure, we calculate the zero-order spectral reflectance as a function of incident angle with numerical methods based on rigorous coupled-wave analysis (RCWA) [23]. The first design is an isolated-particle optical grating composed of SiO_2 rectangular rods with refractive index $n = 1.5$, thickness $d_g = 870$ nm, and period $\Lambda = 1000$ nm. For this design, the band flip is executed for $F = 0.36$, $F = 0.38$, and $F = 0.4$ as depicted in Fig. 1(a). It is seen that for $F = 0.36$, the bandgap is open, and the nonleaky (BIC) edge and the leaky (GMR) edge reside at the upper and lower bands, respectively. By increasing F to 0.38, the band closes, reopening at $F = 0.4$ with the BIC-GMR edges interchanged. Analogous results are obtained for a lattice connected by a sublayer consisting of ZnSe with refractive index $n = 2.5$, $d_g = 100$ nm, $d_h = 500$ nm, and $\Lambda = 1000$ nm. This structure is placed on a glass substrate with $n = 1.5$. Figure 1(b) shows the attendant band flip process under variation of fill factor as $F = 0.3$, $F = 0.48$, and $F = 0.66$.

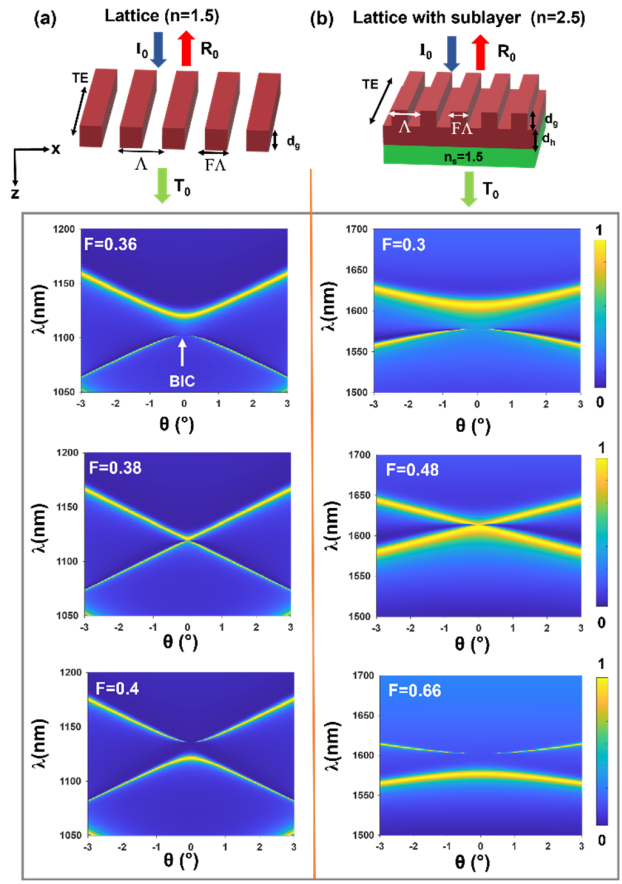

Fig. 1. Displayed are angle–wavelength (θ–λ) zero-order reflectance (R_0) color maps for the (a) lattice with $d_g = 870$ nm, $\Lambda = 1000$ nm, $n = 1.5$ with $F = 0.36$, $F = 0.38$, and $F = 0.4$, (b) lattice with $d_g = 100$ nm, $d_h = 500$ nm, Λ=1000 nm, $n = 2.5$ having $F = 0.3$, $F = 0.48$, and $F = 0.66$. The incident wave is in the TE polarization state with its electric field vector along the grating ridges. Note that the upper (lower) edge refers to shorter (longer) wavelengths as conventional.

The experimental devices consist of a positive photoresist (PR) grating on an Si_3N_4 homogenous layer and a glass substrate. The grating parameters including period, depth, and refractive index are $\Lambda = 1000$ nm, $d_g = 250$ nm, and $n = 1.6$, respectively. The homogenous layer thickness is (d_h) 550 nm with a refractive index of 1.8. Apart from the fill factors, all the designs possess the same materials and parameters. An advantage of this approach is that device etching is avoided, reducing the likelihood of fabrication errors.

The fabrication process of the gratings begins with the deposition of a Si_3N_4 thin film on a cleaned glass substrate using plasma-enhanced chemical vapor deposition (PECVD). The film thickness and refractive index of the film are $d_h = 550.7$ nm and $n = 1.798$, as confirmed by ellipsometry. Thereafter, a 250-nm positive photoresist (Shipley 1813) layer is spin-coated on the film. To improve the adhesion between the PR and Si_3N_4, we spin-coat a thin layer of hexamethyldisiloxane (HDMS) on the film before applying the PR. A 1D grating pattern with a 1000-nm period is then recorded on the PR using laser interferometric lithography (LIL). The lithography system is based on a classic LIoyd-mirror geometry with pattern period easily regulated by

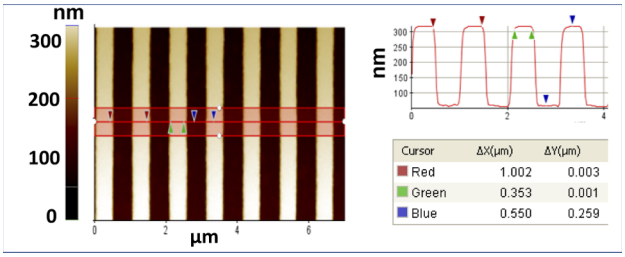

Fig. 2. AFM image showing the grating profile of a representative PR design. The red, green, and blue arrows point out the period, fill factor, and grating depth as $F = 0.353$, $\Lambda = 1002$ nm, $d_g = 259$ nm.

stage rotation. The exposing laser is well-polarized and has a wavelength of 266 nm. The most critical parameter is the fill factor which is controlled by the exposure energy of the laser. By increasing the exposure energy, the fill factors of the grating patterns decrease.

To characterize the fabricated resonant lattices, atomic force microscopy (AFM) is employed to measure the period, grating thickness, and fill factor. Figure 2 depicts the measured parameters for one of the PR gratings with red, green, and blue arrows indicating the period, fill factor, and grating thickness, respectively. This device has Λ=1002 nm, $F = 0.353$, and $d_g = 259$ nm, as shown in Fig. 2. Additional AFM measurements give the parameters related to the second device as $\Lambda = 1002$ nm, $F = 0.48$, and $d_g = 253$ nm, and the third as $\Lambda = 1002$ nm, $F = 0.565$, and $d_g = 260$ nm. Repeated and averaged AFM measurements with error ~±1% reveal that the fabricated PR gratings possess nearly the same fill factors and periods as in the simulated designs.

Figure 3 shows the experimental setup used to measure the optical transmission. An optical fiber carries light from a supercontinuum laser source through a collimator. The collimated light then passes through a polarizer. The polarized light is incident on the resonant grating after passing an optical aperture. A detector connected to the optical spectrum analyzer (OSA) quantifies the transmittance diffracted by the grating. A computer collects the data related to the measured transmission.

Transmittance is measured as a function of wavelength with and without the device under test to ascertain the zero-order diffraction efficiency. Thus, the transmittance is measured for a wavelength span of 1550 nm to 1700 nm. The supercontinuum laser outputs a continuous spectrum covering the wavelength range of interest. The OSA with resolution of 0.05 nm delivers the transmission spectrum. This measurement is done for each angle of incidence in the range $-1° < \theta < 1°$ on a grid with $\Delta\theta = 0.01°$. The transmittance related to each of these

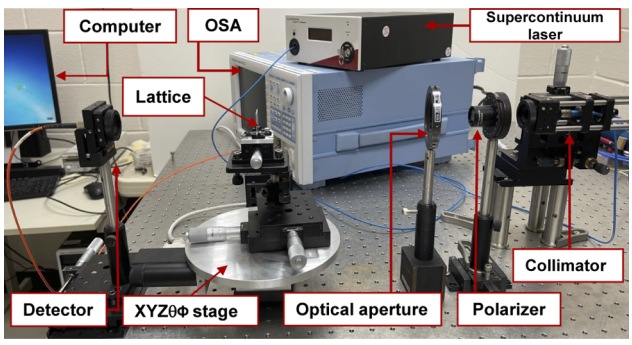

Fig. 3. Photograph of the lattice-dynamics measurement setup.

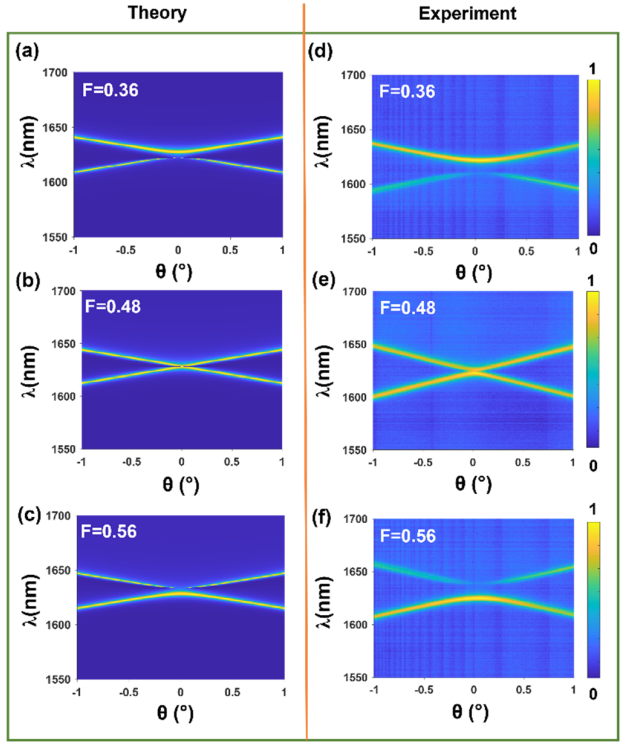

Fig. 4. Band flip demonstration for the subwavelength grating structures showing the band structures for $F = 0.36$, $F = 0.48$, and $F = 0.56$. (a)–(c) Theoretical R_0 results are calculated by rigorous coupled-wave analysis. (d)–(f) Experimental R_0 data measured with the optical spectrum analyzer and plotted in MATLAB. The color bar represents normalized experimental reflectance.

angles is measured showing two peaks at nonzero incidence. The reflection spectrum is formed by using $R_0 = 1 - T_0$. To plot the angle-dependent spectral reflection map, the corresponding data is imported into MATLAB for processing. This procedure is performed for the three fabricated devices.

Figure 4 depicts theoretical and corresponding experimental results. The simulation results are shown in Figs. 4(a)–4(c) for $F = 0.36$, $F = 0.48$, and $F = 0.56$, respectively. Figures 4(d)–4(f) demonstrate the experimental data for the same structures. This figure shows that the fabricated devices exhibit band structure and band flip effects consistent with simulation. Moreover, the experimental data illustrates the transition of the nonleaky BIC state and the leaky GMR state across the bandgap.

For added detail and clarity, reflectance spectra of the lattice design with $F = 0.56$ are provided here for an improved comparison between the numerical and experimental data. The numerical and experimental bandgaps for $F = 0.56$ are compared in Figs. 5(a) and 5(b) in increased resolution with red dashes denoting experiment. Figures 5(c) and 5(d) show zero-order reflectance for angles of $\theta = 0°$ and $\theta = 1°$, respectively. The theoretical reflectance spectra for $\theta = 0°$ in Fig. 5(c) show $R_0 = 1$ at $\lambda = 1.630$ µm, whereas the experimental data shows an $R_0 = 0.86$ at 1.625 µm. For $\theta = 1°$ the simulation shows two resonant peaks appearing at $\lambda = 1.615$ µm and $\lambda = 1.647$ µm providing 100% reflection; nearby, at $\lambda = 1.610$ µm and $\lambda = 1.655$ µm, ~60% reflection is detected in the experimental results, as presented in Fig. 5(d).

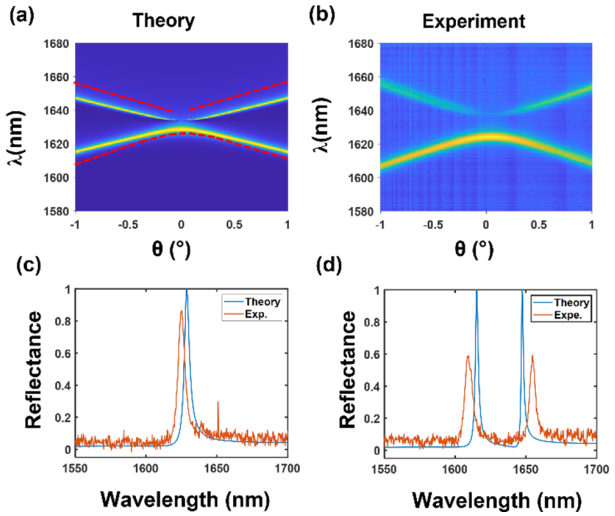

Fig. 5. Comparison of (a) simulation and (b) experimental band flip for the PR grating after band closure ($F = 0.56$). Simulation results and experimental data for R_0 are shown in blue and orange plots, respectively for (c) $\theta = 0°$, (d) $\theta = 1°$.

The deviations in efficiency between the ideal element used in the simulation and experiment arise mainly due to the differences in the interrogating waves. A plane wave source is used in the RCWA simulations, whereas the beam produced by the supercontinuum laser shown in Fig. 3 has a Gaussian shape with a diameter of ~1 mm at $\lambda = 1100$ nm; this finite-width beam is not modeled in Figs. 5(c) and 5(d).

In summary, we provide an experimental demonstration of band flips and bound-state transitions in one-dimensional dielectric photonic lattices. Whereas the band dynamics were previously explained using analytical and numerical models, we review the detailed physical processes responsible for BIC/GMR edge positioning as well as the band closure point providing a clear view of the pertinent physics. In this study, subwavelength optical lattices composed of a photoresist grating, Si_3N_4 sublayer, and a glass substrate with distinct fill factors are designed, fabricated, and characterized. The corresponding reflectance spectra are subsequently measured. In the end, the theoretical results and experimental data are compared depicting a reasonable match.

Funding. National Science Foundation (ECCS-1809143).

Acknowledgment. Parts of this research were conducted in the UT Arlington Shimadzu Institute Nanotechnology Research Center.

Disclosures. The authors declare no conflicts of interest.

Data availability. The data that support the findings of this Letter are available from the corresponding author upon reasonable request.

REFERENCES

1. C. Kittel, *Introduction to Solid State Physics*, 4th ed. (Wiley 1971).
2. E. Yablonovitch, J. Opt. Soc. Am. B **10**, 283 (1993).
3. J. D. Joannopoulos, R. D. Meade, and J. N. Winn, *Photonic Crystals: Molding the Flow of Light* (Princeton University Press, 1995).
4. K. M. Ho, C. T. Chan, and C. M. Soukoulis, Phys. Rev. Lett. **65**, 3152 (1990).
5. K. M. Leung and Y. F. Liu, Phys. Rev. Lett. **65**, 2646 (1990).
6. E. Degirmenci and P. Landais, Appl. Opt. **52**, 7367 (2013).
7. S. Joseph, S. Sarkar, S. Khan, and J. Joseph, Adv. Opt. Mater. **9**, 2001895 (2021).
8. P. Vincent and M. Neviere, Appl. Phys. **20**, 345 (1979).
9. I. A. Avrutsky and V. A. Sychugov, J. Mod. Opt. **36**, 1527 (1989).
10. S. Wang and R. Magnusson, Appl. Opt. **32**, 2606 (1993).
11. S. Peng and G. M. Morris, J. Opt. Soc. Am. A **13**, 993 (1996).
12. D. Rosenblatt, A. Sharon, and A. A. Friesem, IEEE J. Quantum Electron. **33**, 2038 (1997).
13. Y. Ding and R. Magnusson, Opt. Express **12**, 1885 (2004).
14. Y. Ding and R. Magnusson, Opt. Express **15**, 680 (2007).
15. D. C. Marinica, A. G. Borisov, and S. V. Shabanov, Phys. Rev. Lett. **100**, 183902 (2008).
16. J. von Neuman and E. Wigner, Phys. Z. **30**, 467 (1929).
17. R. F. Kazarinov and C. H. Henry, IEEE J. Quant. Elect **21**, 144 (1985).
18. S.-G. Lee and R. Magnusson, Phys. Rev. B **99**, 045304 (2019).
19. S. R. K. Rodriguez, A. Abass, B. Maes, O. T. A. Janssen, G. Vecchi, and J. Gómez Rivas, Phys. Rev. X **1**, 021019 (2011).
20. T. K. Hakala, H. T. Rekola, A. I. Väkeväinen, J. P. Martikainen, M. Nečada, A. J. Moilanen, and P. Törmä, Nat. Commun. **8**, 13687 (2017).
21. V. Tretnak, U. Hohenester, J. R. Krenn, and A. Hohenau, J. Phys. Chem. C **124**, 2104 (2020).
22. V. G. Kravets, A. V. Kabashin, W. L. Barnes, and A. N. Grigorenko, Chem. Rev. **118**, 5912 (2018).
23. T. K. Gaylord and M. G. Moharam, Proc. IEEE **73**, 894 (1985).